The Effects of Finish Rolling Temperature and Cooling Interrupt Conditions on Precipitation in Microalloyed Steels Using Small Angle Neutron Scattering

J.B. WISKEL, D.G. IVEY, and H. HENEIN

Small angle neutron scattering (SANS) was used to quantify the precipitate characteristics (*i.e.*, mean precipitate size, number of precipitates, and distribution broadening) in X-70 and X-80 pipeline steel and in grades 80 and 100 microalloyed steel plate. The precipitate distributions measured for the different steels were correlated with the finish rolling temperature (FRT) and cooling interrupt temperature (CT) as a means of identifying processing conditions that may enhance fine precipitate evolution. It was observed that for some combinations of processing conditions two distinct precipitation events—based on size of the precipitates—were occurring. The first precipitation event (larger size) was strongly associated with the FRT, where a decrease in the mean precipitate radius with decreasing FRT was observed. The second (finer size) precipitation event was affected by both the CT and the FRT. Both the size and volume of the second precipitation event was observed to decrease with decreasing CT. The precipitate distribution predicted from the SANS data for grade 100 steel compared favorably to precipitation data obtained from particle counting analysis conducted with a transmission electron microscopy (TEM).

DOI: 10.1007/s11663-007-9104-8

I. INTRODUCTION

TRADITIONAL strengthening mechanisms for high-strength microalloyed steels used in pipelines include grain refinement, dislocation strengthening, and precipitation strengthening. Precipitates that are produced in high-strength microalloyed steels can include Ti(C,N), Nb(C,N)[1–3] and other phases depending on the exact composition of the steel. In addition to composition, the processing parameters associated with thermomechanical controlled processing (TMCP) of these steels, including casting, the reheating process, rough rolling conditions, finish rolling conditions, and cooling conditions, all can affect the size and number of precipitates that form. However, to achieve any significant amount of strengthening *via* precipitation, precipitate diameters should be on the order of 5 nm[1] in diameter. Thus, an understanding of the relationship between the number density (*i.e.*, distribution) of fine nano-size precipitates that form and their relation to processing is essential for the production of higher-strength microalloyed pipeline steels.

Precipitation events during thermomechanical processing can be grouped according to which stage in the TMCP process the precipitates form.[6] In a very simplistic categorization, large ($>0.5\ \mu$m), primarily TiN, precipitates form during the solidification process and subsequent cooling to the reheat furnace temperature, medium- size Nb,Ti(C,N) precipitates in the size range from 50 to 500 nm form during the hot rolling schedule and very fine precipitates (<10 nm) form during and after laminar cooling.[2–4]

For many commercial grades of microalloyed steel (*e.g.*, containing Nb), the fine precipitates that form are typically Nb-rich carbides.[6] However, depending on the exact composition of other alloying elements (*e.g.*, Mo, Cr) these fine precipitates may include Mo[6] or have an entirely different composition (*e.g.*, Cu-rich precipitates).

The number and size distribution (which affects strengthening) of the fine precipitates (<10 nm) is a complicated function of many factors including the nonequilibrium amount of alloying elements in solution (*e.g.*, Nb) prior to laminar cooling[7] and processing conditions. The fine precipitates typically form at the austenite to ferrite transformation interface (depending on cooling rate)[2,22] or in the ferrite following transformation.[2] For the industrial laminar cooling system used (nominal cooling rates are 15 °C/s), interphase precipitation maybe limited.[5] Therefore, specific processing conditions that may influence the size distribution of these fine precipitates can include finish rolling temperature (FRT) and cooling interrupt temperature (CT).

In particular, CT can have a profound effect on the number, size, and type of fine precipitates as the nucleation and growth of these precipitates are a strong function of temperature in the ferrite phase.[8] Theoretical calculations regarding the fine precipitation event (*i.e.*, nucleation and growth) have been undertaken[20] but direct analysis of the fine precipitate size distribution in commercially processed steels is limited.

J.B. WISKEL, F.S.O., D.G. IVEY, Professor, and H. HENEIN, Professor, are with the Department of Chemical and Materials Engineering, University of Alberta, Edmonton, AB, Canada. Contact e-mail: bwiskel@ualberta.ca

Manuscript submitted October 4, 2007.
Article published online December 8, 2007.

A number of analytical techniques exist by which fine precipitates in low alloyed steels can be analyzed; these include scanning electron microscopy (SEM), transmission electron microscopy (TEM),[3,4,9,10] small angle x-ray scattering (SAXS),[10,11] and small angle neutron scattering (SANS).[9,12–14] Traditional SEM is generally limited to large size precipitates (> 50 nm), although field emission SEM has the capabilities of examining finer precipitates (< 10 nm). The TEM analysis has been widely used to provide direct information on the composition, morphology, and size of individual precipitates, the spatial distribution of these precipitates, and, to a lesser extent the precipitate size distribution. These precipitates characteristics have been obtained from samples that have been either electro-polished samples[5,6,9–11,13] (*i.e.*, precipitates remain in matrix) or extracted *via* a carbon replica technique.[5,6] However, TEM analysis does not lend itself easily to volume fraction determination, due to the projection of a three-dimensional structure into two dimensions. The SAXS has been used to study fine precipitation in Fe. However, SAXS analysis of precipitates in steel has generally been limited to experimental alloys or simple commercial alloys in which the precipitate composition is well known.[10,11]

The SANS is a versatile technology for quantifying the size distribution of precipitates, whose size is on the order of 1 to 100 nm, and its application to microalloyed steels would complement the techniques previously discussed particularly in quantifying the size, volume fraction, and distribution of the fine precipitates. The SANS has been used to characterize the precipitation behavior in steels including the following:

(1) copper precipitates in a Fe-Cu binary system,[12]
(2) NbC precipitates in experimental Fe-Nb-C alloys,[13]
(3) Nb(C,N) precipitates at a high temperature (900 °C to 1200 °C),[14]
(4) M_2C carbides in high-alloy Co-Ni steels,[15] and
(5) precipitates in maraging steels.[16]

Challenges associated with applying SANS to commercially produced microalloyed steels include (1) the low volume fraction of the very fine precipitates and (2) the wide range of precipitate sizes (see earlier discussion) resulting from precipitation events associated with discrete stages in the TMCP process. Also, variations in through thickness precipitation behaviour due to segregation or differences in processing histories must be considered when analyzing commercially produced alloys.

The work presented in this article will apply SANS to commercial microalloyed pipeline steels including X-70 and X-80 (American Petroleum Institute, API specifications) and to plate steel grade 80 and grade 100. The aim is to correlate the size distribution of the very fine precipitates (on the order of 5 nm) present in these steels to the normalized FRT and normalized CT, and to the ratio of Nb to C and the total percent of Cu present. The results of the SANS analysis of the grade 100 steel will be used to validate the precipitate analysis technique by comparing TEM analysis of the grade 100 with the SANS results.

Table I. Steels Analyzed

Steel	Pct C	Pct Nb	Pct Ti	Pct Cu	FRT	CT
X80-462	0.03	0.09	0.013	0.27	0.94	1.04
X80-A4B	0.04	0.09	0.017	0.34	1.05	0.93
X80-B4F	0.05	0.08	0.010	0.15	1.00	1.00
X80-A4F	0.05	0.04	0.010	0.15	1.00	0.90
X70-AOL	0.043	0.08	0.025	0.24	1.01	0.64
X70-AOJ	0.045	0.07	0.019	0.22	1.00	0.63
G80-B3A	0.056	0.089	0.032	0.41	1.07	1.04
Grade 100	0.06	0.09	0.060	0.40	1.07	1.09

II. EXPERIMENTAL METHODOLOGY AND DATA ANALYSIS

A. *Samples*

The compositions of the steels studied in this work are summarized in Table I. All the steel samples have relatively low carbon contents (< 0.06 wt pct), a Nb content less than 0.10 wt pct, and a relatively low Ti content (except for the grade 100 sample at 0.060 wt pct). Other alloying elements present in these steels may include Cr, Ni, and Mo to varying weight percentages but typically less than 0.2 wt pct. The composition of Cu has been included due to the possibility of Cu precipitate formation at compositions greater than 0.15 wt pct. Also included in Table I are the process variables deemed important in the generation of the fine ($\approx$5 nm) precipitates—the FRT and the CT (both normalized). In general, except for the differences in FRT, CT, and composition, each group of steels (*e.g.*, X-80) was processed in a similar manner.

The SANS samples ranging in thickness between 4.5 and 6.6 mm—with a surface area of 10 × 10 mm—were extracted both above (T) and below (B) the centerline of the original skelp material. The samples were prepared to avoid including material from both the centerline (where possible segregation may alter the nominal composition) and the surface of the skelp. The samples were mechanically polished to 1.0-μm diamond and were oriented in the SANS neutron beam with the rolling plane (*i.e.*, rolling surface) perpendicular to the beam orientation.

B. *SANS Testing*

The SANS experiments were conducted on the NG-3 Neutron Guide at the National Institute of Standards Center for Neutron Research.[17] Neutrons were monochromated by a velocity selector to a mean wavelength of 0.54 nm with the wavelength spread being $\Delta\lambda/\lambda = 10$ pct. The samples were magnetized to saturation in a 2 Tesla magnetic field. Three detector distances (1.9, 5.55, and 13.65 m) were used, giving access to scattering vector (**Q**) values ranging from 0.023 to 2.1 nm, where the value of **Q** is calculated as follows:

$$\mathbf{Q} = 4 \cdot \pi \cdot \sin(\theta/2)/\lambda \qquad [1]$$

where θ is the scattering angle. The scattered neutrons were recorded with a 640 mm × 640 mm ^{3}He position sensitive proportional counter with a 5 × 5 mm resolution.

The measured neutron beam intensity at each **Q** value was converted to a differential scattering cross section ($d\Sigma/d\Omega$) value by scaling the measured neutron beam intensity with sample thickness and transmission, response of the detector, and background scattering.[15] Due to the application of the magnetic field (all the precipitates were considered nonmagnetic),[16] the vertical differential scattering cross section $d\Sigma/d\Omega_V$ is a combination of both nuclear and magnetic scattering components, whereas the horizontal differential scattering cross section $d\Sigma/d\Omega_H$ is comprised only of nuclear scattering. Figure 1 shows the variation of $d\Sigma/d\Omega_V$ and $d\Sigma/d\Omega_H$ as a function of the scattering vector **Q**. The difference in magnitude between the two curves is the contribution of the magnetic scattering component. As the exact composition of the precipitates that form in these commercial alloys is not known, only the magnetic differential scattering cross section will be considered in this work.

The magnetic differential scattering cross section for each sample tested was obtained by subtracting the value of the horizontal (*i.e.*, nuclear) differential scattering cross section measured at $\alpha = 0$ from the value of the vertical (*i.e.*, nuclear + magnetic) differential scattering cross section measured at $\alpha = \pi/2$ for a scattering vector value, where α is the angle between the scattering vector and the magnetic field.[16] In this work, the respective scattering magnitudes at each **Q** were averaged over $\alpha \pm 10$ deg. Figure 2 is a plot of the calculated magnetic differential scattering cross section for sample X-80-462-T as a function of **Q**. The magnetic differential scattering cross section calculated for each sample was used for all subsequent size distribution calculations and analysis.

The magnetic scattering data shown in Figure 2 include the scattering effects of not only the fine precipitates (5 nm) of interest, but also of larger precipitates that occur in these microalloyed steels. Therefore, in the analysis of the magnetic differential scattering cross section data generated for each sample, an additional assumption is made that the precipitates (in a commercial microalloyed steel) do not form a continuous distribution of particle sizes but discrete

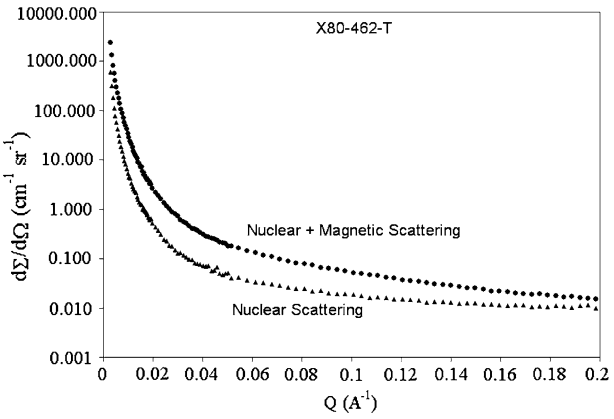

Fig. 1—Differential scattering cross section as a function of scattering vector for both nuclear and nuclear + magnetic scattering for sample X-80-462-T.

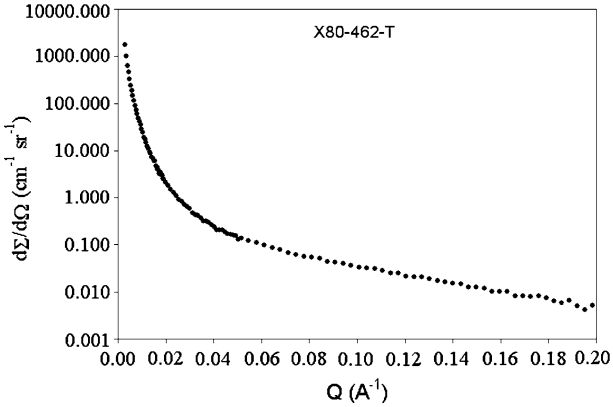

Fig. 2—Magnetic component of the differential scattering cross section as a function of scattering vector for sample X-80-462-T.

precipitate distributions associated with the individual stages of the TMCP processing. As discussed earlier, TEM[6] analysis of both X-70 and X-80 microalloyed steels has identified groupings of precipitates associated with the different TMCP stages, including (1) precipitates in the size range from 500 to 100 nm (formed during the rough rolling operation), (2) precipitates in the 30- to 50-nm range (during finish rolling), and (3) fine precipitates (less than 20 nm with an average size of 5 nm for X-70 and 15 nm for X-80) that are generated during the transformation and cooling interrupt operations.

Based on the concept of discrete size distributions, the effect on the differential magnetic scattering cross section of the larger precipitates (*i.e.*, >30 nm) was removed from the scattering associated with the very fine precipitates (around 5 nm). This was done by assuming that the contribution to the magnetic differential scattering cross section of these larger particles followed the Porod behavior[18,23] (*i.e.*, $d\Sigma/d\Omega \propto 1/\mathbf{Q}^4$) at larger **Q** values, whereas the finer precipitates are following Guinier behavior. The effect of the Porod scattering behavior for the large precipitates was removed from the measured magnetic differential scattering cross section by subtracting an extrapolation (numerically fitted to the data) of the Porod behavior at scattering angles $\mathbf{Q} < 0.3$ nm. An example of this scattering adjustment is illustrated in Figure 3, where the solid line represents the estimated Porod behavior of the relatively large precipitates. The resultant magnetic differential scattering cross section (following subtraction of the Porod scattering of the large particles) is shown in Figure 4 for sample X-80-462-T.

C. *Fundamental Scattering Analysis*

The differential scattering cross section for a dilute system can be calculated as follows:[16]

$$d\Sigma/d\Omega = \Delta\rho_m^2 \cdot \int_0^\infty V(R)^2 \cdot N(R) \cdot |F(\mathbf{Q},R)|^2 \cdot |S(\mathbf{Q},R)| \cdot dR \qquad [2]$$

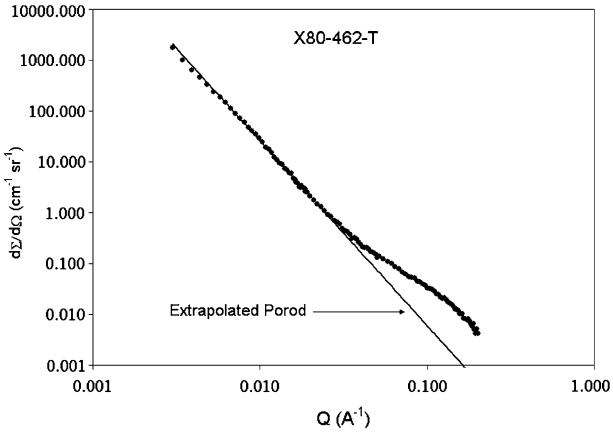

Fig. 3—Comparison of extrapolated Porod behavior and measured magnetic differential scattering cross section for sample X-80-462-T.

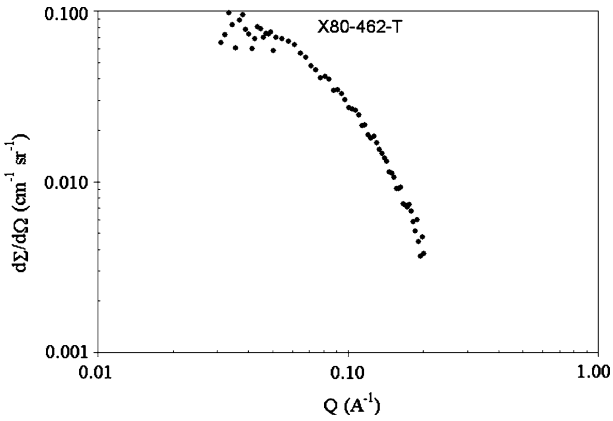

Fig. 4—Modified (following subtraction of extrapolated Porod behavior) differential scattering cross section of magnetic scattering for sample X-80-462-T.

where R is the radius of any precipitate, $\Delta\rho_m$ is the magnetic scattering length density difference that is calculated to have a value of $5.0 \times 10^{10}/\text{cm}^2$ (for the compositions shown in Table I), $V(R)$ is the volume of a particle of radius R, $N(R)$ is the number of scattering bodies per volume with radius R, and $F(\mathbf{Q},R)$ is the form factor that for spherical particles is calculated using the following equation:

$$|F(\mathbf{Q},R)| = 3\frac{\sin(\mathbf{Q}\cdot R) - \mathbf{Q}\cdot R\cdot\cos(\mathbf{Q}\cdot R)}{(\mathbf{Q}\cdot R)^3} \quad [3]$$

Though ellipsoid or rod-type fine precipitates have been observed in laboratory manipulated samples of low-alloy steel,[5,11,13] TEM analysis[6] of the commercial variety of these steels has indicated primarily spherical precipitates (of the sizes being studied), which validates Eq. [3]. The term $S(\mathbf{Q},R)$ is the interparticle structure factor, and for randomly-oriented dilute systems, it is assumed to be 1.

A normalized value for $N(R)$ was calculated using the density function of a log-normal precipitate size distribution of the following form:[10,13,16]

$$N(R) = N_o\left(\frac{1}{\alpha\cdot R\cdot\sqrt{2\cdot\pi}}\cdot\exp\left[-\frac{1}{2}\cdot\left(\frac{\ln(R/R_o)}{\alpha}\right)^2\right]\right) \quad [4]$$

where N_o is the total number of scattering bodies in the distribution per volume (μm^3), R_o is the precipitate radius at the maximum of the distribution, and α is a fitting parameter related to the width of the distribution *via* the relationship

$$\alpha = \frac{\beta}{R_o} \quad [5]$$

where β is the width of the distribution.

Equations [2] through [4] were applied to the SANS data (*e.g.*, Figure 4) to predict the values N_o, R_o, and α for each sample by numerically solving the integral in Eq. [3] while simultaneously solving for N_o, R_o, and α using a nonlinear Newton–Raphson technique that minimizes the error between the measured differential scattering cross section value and the value calculated *via* Eq. [3] for each $\mathbf{Q}$ value.

D. *Calculation of N_o, R_o, and α for a Single Log-Normal Distribution*

Figure 5 is a Kratky plot comparing the measured differential scattering values for X-80-462-T to the predicted values (derived using the methodology previously described). Included in Figure 5 are the calculated values for N_o, R_o, and α and the calculated volume fraction (based on the total number of particles) for this distribution. The predicted log-normal average radius R_o (1.07 nm) is on the same order of magnitude as the Guinier radius (R_g) value (1.53 nm) predicted using the following equation:

$$R_g = \frac{A}{\mathbf{Q}_{\max}} \quad [6]$$

where $A = 1.7$[10] and $\mathbf{Q}_{\max}$ is the value of $\mathbf{Q}$ at the peak ($\approx$1.11 nm^{-1}) in Figure 5.

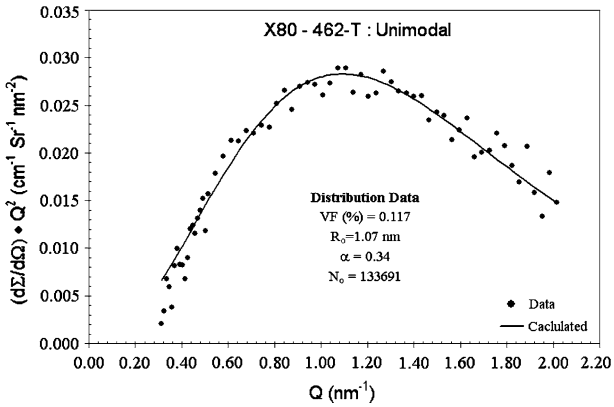

Fig. 5—Measured and predicted (unimodal log-normal distribution) differential scattering cross sections for X-80-462-T.

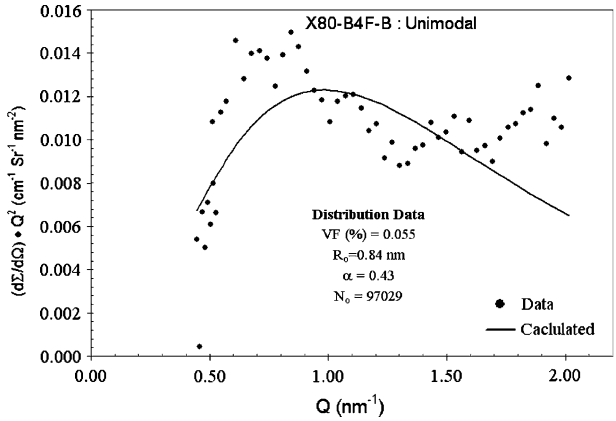

Fig. 6—Measured and predicted (unimodal log-normal distribution) differential scattering cross sections for X-80-4BF-B.

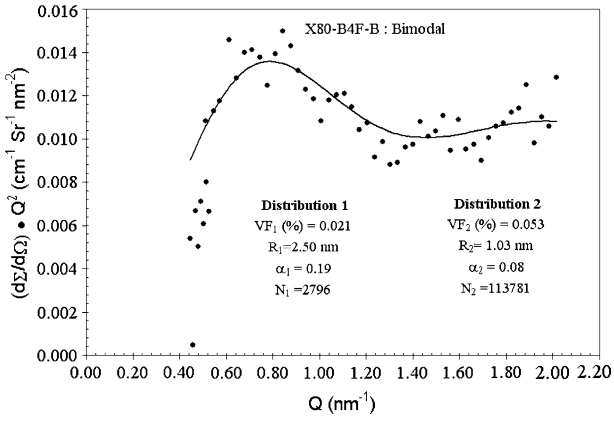

Fig. 7—Measured and predicted (bimodal log-normal distribution) differential scattering cross sections for X-80-4BF-B.

E. *Calculation of N_o, R_o, and α for a Bimodal Log-Normal Distribution*

The predicted differential scattering cross section—calculated using a single log-normal distribution of precipitates—is compared to the measured value for X-80-B4F-T in Figure 6. Unlike Figure 5, where the correspondence between the predicted and measured differential scattering cross section was reasonably good, Figure 6 exhibits a marked deviation of the predicted behavior from the measured. This deviation may indicate the existence of a bimodal fine precipitate population (*i.e.*, the occurrence of two distinct fine precipitation events).

The calculations for X-80-B4F-B were repeated but were undertaken using a bimodal precipitate distribution (*i.e.*, two distinct distributions). The number of variables used for the calculation included two sets of distribution data (R_1, N_1, and α_1) and (R_2, N_2, and α_2), where the subscript 1 indicates the distribution of one set of precipitates and the subscript 2 the behavior of a second precipitation distribution. A comparison between the measured and predicted differential scattering cross sections calculated using a bimodal distribution of fine precipitates is shown in Figure 7. Unlike Figure 6, the bimodal distribution calculations show a reasonably good fit with the measured data.

F. *Comparison of SANS results with TEM Analysis for Grade 100*

The precipitates in the grade 100 material were examined using a TEM.[19] This microscopy work included manual counting of the size and number of the fine precipitates in a carbon replica film taken from this steel. The normalized (volume of carbon replica was not known) size distribution values observed are compared to the predicted size distribution values obtained with SANS in Figure 8. Included in Figure 8 are the bimodal precipitate distribution variables used to calculate the normalized SANS distribution. In general, the relative distributions compare well with each other confirming the veracity of the SANS methodology previously described.

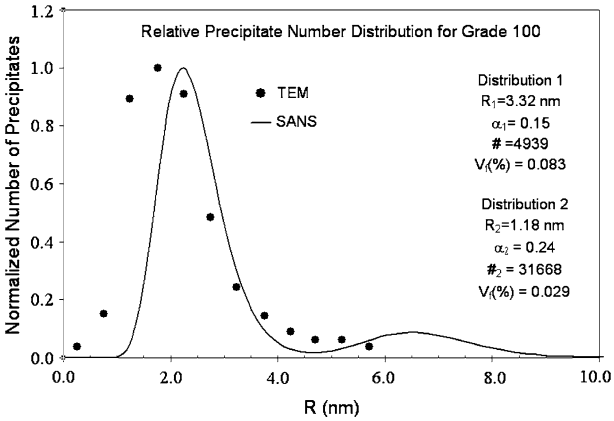

Fig. 8—Normalized number distribution of precipitates measured by TEM (using carbon replicas)[19] and predicted by SANS for grade 100.

III. RESULTS AND DISCUSSION

The SANS data analysis described in the previous section was repeated for all the samples listed in Table I. The results of the analysis are tabulated in Table II and include the log-normal bimodal precipitate distribution parameters, the number of particles per volume, the volume fraction of each size distribution, and the total volume fraction of the fine precipitates. To maintain consistency, the SANS scattering calculations for both X-80-462-T and X-80-462-B were repeated using a bimodal distribution. The justification (in terms of fit between the measured and the calculated differential scattering cross section) of the unimodal *vs* bimodal for these two samples is not as strong as in the other samples, however, this assumption was undertaken to ensure consistency in the analysis that follows. The data points for both X-80-462-T and X-80-462-B are explicitly noted in all the figures. The size distribution data presented in Table II are analyzed in conjunction with the processing data for each sample (Table I), including the effects of FRT, CT, and composition on the amount and size of fine precipitates that form.

In general, many factors will effect the precipitation of nano-sized particles, including temperature, applied

Table II. Calculated Precipitate Distribution Characteristics

Sample	R_1 (nm)	α_1	$\#_1$	VF_1 (Pct)	R_2 (nm)	α_2	$\#_2$	VF_2 (Pct)	VF_{total} (Pct)
X80-462T	2.05	0.23	3979	0.018	1.19	0.25	100350	0.096	0.114
X80-462B	2.07	0.3	4401	0.024	1.22	0.25	89350	0.091	0.115
X80-A4BT	3.20	0.18	1003	0.016	1.06	0.06	120128	0.051	0.067
X80-A4BB	3.50	0.17	558	0.011	0.90	0.06	115692	0.036	0.047
X80-B4FT	2.50	0.18	2760	0.02	1.01	0.08	113728	0.05	0.070
X80-B4FB	2.50	0.19	2796	0.021	1.02	0.08	113781	0.053	0.074
X80-A4FT	2.14	0.25	1861	0.051	1.02	0.07	106619	0.049	0.100
X80-A4FB	2.50	0.33	1096	0.012	0.98	0.10	80727	0.036	0.048
X70-A0JT	2.59	0.21	1472	0.013	0.93	0.06	90139	0.031	0.044
X70-A0LT	2.60	0.22	666	0.006	0.8	0.06	101466	0.022	0.028
G80-B3AT	2.73	0.21	3926	0.041	1.27	0.07	53935	0.047	0.088
G80-B3AB	2.83	0.22	3405	0.04	1.22	0.07	57303	0.044	0.084
G100	3.32	0.15	4939	0.083	1.18	0.24	31668	0.029	0.112

#: Number of precipitates.

strain, composition, and so forth;[20] therefore, the lack of a definite correlation of the precipitation distribution data with a single specific processing variable (*e.g.*, FRT) should not be construed as this variable having no effect. The objective of the following discussion is to establish what variable(s) have both a direct and significant effect on the precipitation phenomena and use this information to establish guidelines in the processing of these steels.

A. *Effect of FRT*

The values of R_1 and R_2 are plotted as a function of the normalized FRT in Figures 9 and 10, respectively, for all the steels tested. It is observed in Figure 9 that R_1 increases in value as FRT increases. The trend observed suggests that the first distribution precipitation event (*i.e.*, the larger of the fine precipitates) is associated with the finish rolling practice. The larger mean size observed with increasing FRT can be qualitatively linked with increased coarsening of these precipitates at the higher temperatures at which they form.

Conversely, in Figure 10 (R_2 *vs* FRT), there is not a definite trend between the size of the precipitate for the second precipitate distribution and the FRT. This data suggest that FRT may have only secondary effect on the second distribution of precipitates that form. As will be shown following, a combination of FRT and CT have a strong influence on the size of the second precipitation distribution.

Figures 11 and 12 compare the volume fraction of each precipitation distribution (VF_1 and VF_2) with FRT. No direct correlation of volume fraction (of either size distribution) with FRT is apparent. As FRT is an indicator of temperature during the entire finish rolling process and, hence, solubility of the alloying elements, the lack of a correlation is surprising. However, it is more likely that other variables are influencing volume fraction amounts in conjunction with FRT.

B. *Effect of CT*

The value of R_1 is plotted *vs* the normalized CT in Figure 13. The lack of a distinctive correlation between R_1 and CT suggest that the (first) distribution of precipitates is not associated with the cooling interrupt process. However, as observed in Figure 9, R_1 is directly affected by the FRT and, hence, precipitation of the first (larger distribution) is occurring during the final stages of rolling and not during cooling.

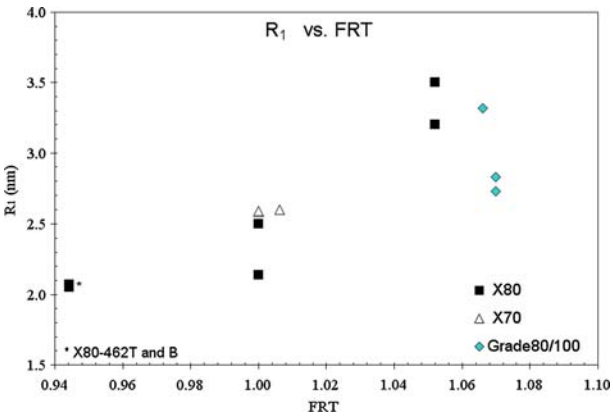

Fig. 9—Log-normal radius (R_1) for X-70, X-80, and grades 80 and 100 as a function of normalized FRT.

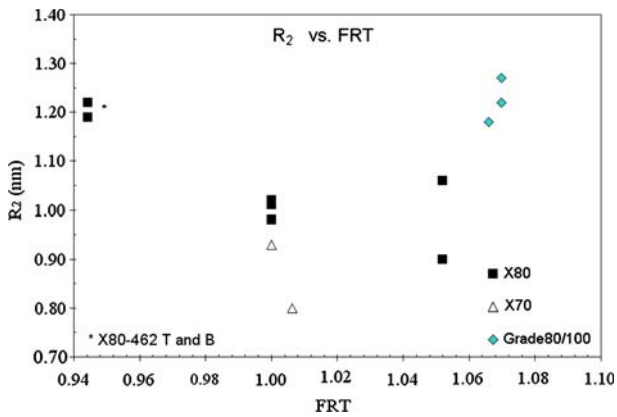

Fig. 10—Log-normal radius (R_2) for X-70, X-80, and grades 80 and 100 as a function of normalized FRT.

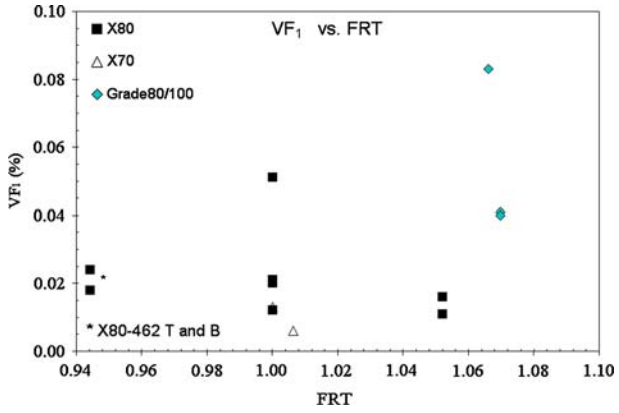

Fig. 11—Volume fraction (VF_1) for X-70, X-80, and grades 80 and 100 as a function of the normalized FRT.

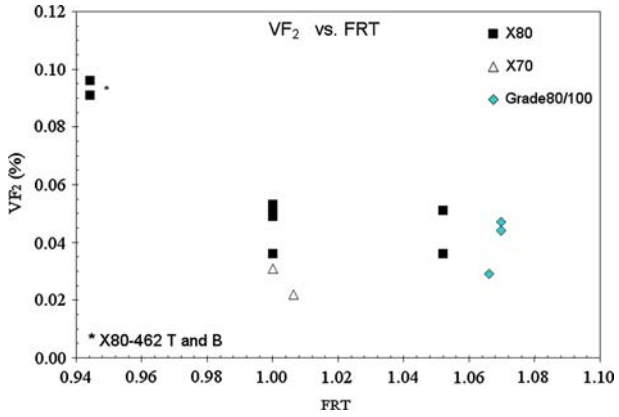

Fig. 12—Volume fraction (VF_2) for X-70, X-80, and grades 80 and 100 as a function of the normalized FRT.

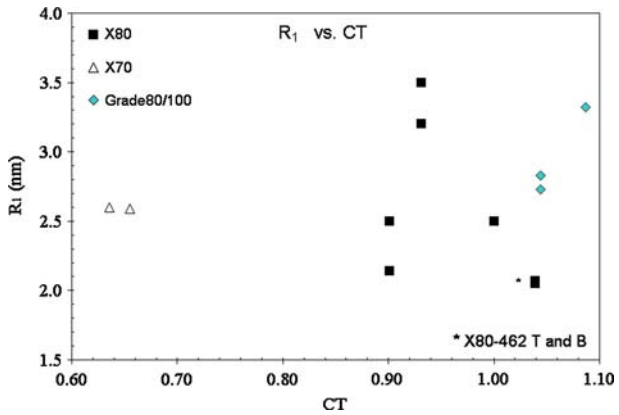

Fig. 13—Log-normal radius (R_1) for X-70, X-80, and grades 80 and 100 as a function of the normalized CT.

A plot of R_2 as a function of CT is shown in Figure 14. Unlike, the R_1 *vs* CT figure, a definite decrease in the log-normal mean radius (R_2) with decreasing CT is observed. This correlation would indicate that this second precipitation event is strongly influenced by the CT. From an understanding of

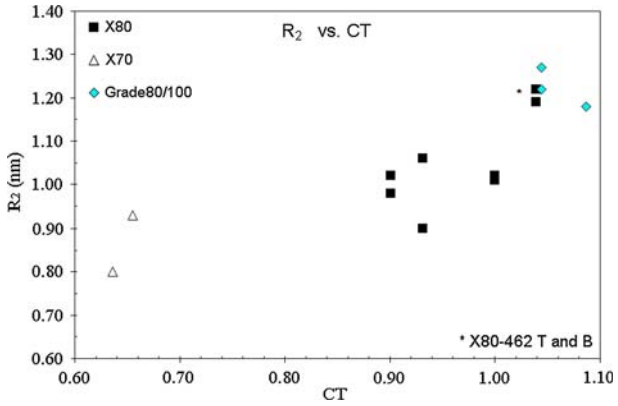

Fig. 14—Log-normal radius (R_2) for X-70, X-80, and grades 80 and 100 as a function of the normalized CT.

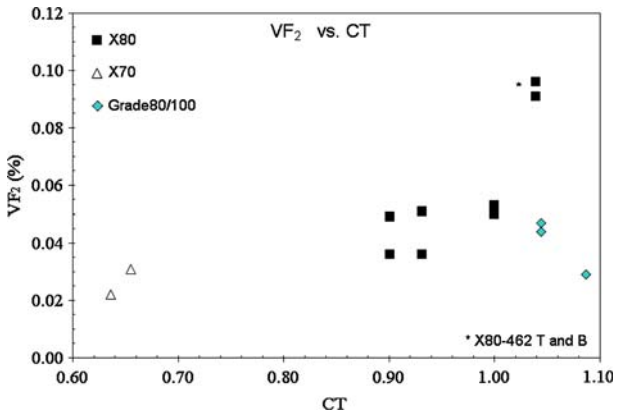

Fig. 15—Volume fraction (VF_2) for X-70, X-80, and grades 80 and 100 as a function of the normalized CT.

nucleation and growth of precipitates in ferrite,[20] the lower the value of CT, the smaller the overall size of precipitate that forms (*i.e.*, less coarsening of these fine precipitates would occur due to the lower temperature). However, CT can also affect the amount of the fine precipitates that form.

Figure 15 plots the volume fraction (VF_2) of the second size distribution as a function of CT. It is observed in this figure that the volume fraction of fine precipitates decreases with decreasing CT. This suggests a kinetic limitation on the formation of these fine precipitates as the precipitation temperature (*i.e.*, CT) is lowered. Thus, processing conditions that are manipulated to produce very fine precipitates (*i.e.*, smaller-size precipitates) may be counter productive toward the objective of increasing strength, as the volume fraction of the precipitates that forms also decreases.

C. *Combined Effect of FRT and CT on Precipitation*

It is likely that more than one process variable can affect the precipitation events. To illustrate this effect, the values of R_2 and VF_2 are plotted as a function of the ratio of CT to FRT. Though the value of CT to

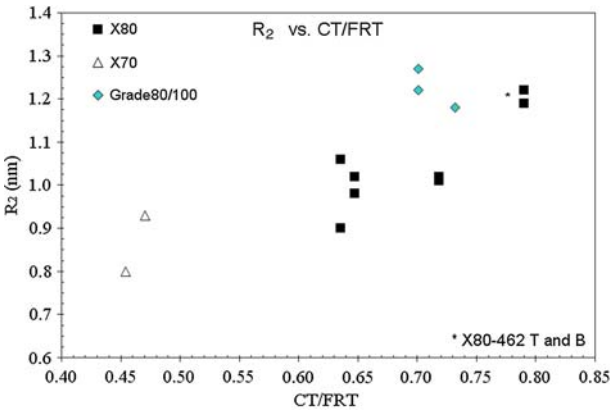

Fig. 16—Log-normal radius (R_2) for X-70, X-80, and grades 80 and 100 as a function of the ratio of CT to FRT.

FRT does not have a specifically recognized phenomenological effect on precipitation, it does include in a single variable the effects of both FRT and CT on precipitation. Figure 16 shows the effect of this ratio on R_2. It is observed that R_2 decreases as CT to FRT—a combination of a low CT value and a high FRT—value results in a lower R_2 value. A plot of VF_2 *vs* CT to FRT (Figure 17) exhibits a similar trend indicating the dependence of fine precipitation on both CT and FRT.

A logical extension of this multiple variable effect type of analysis would be the application of a multiple linear regression correlating the effects of all parameters (*e.g.*, the effect of the percentages of Nb, C, Ti, Cu, and FRT and CT on a size distribution variable (*e.g.*, R_2)). The drawback of such a method is that it imposes a linear relationship between the precipitation event and individual variables and ignores higher order effects or confounding effects of the variables. The net result of a multiple linear regression (using normalized data) was that FRT was observed (*via* the coefficient magnitude) to have the largest effect on all the variables (i.e. VF_1, R_1, VF_2, and R_2).

1. *Unimodal vs Bimodal*

The anomaly in the SANS analysis has been the X-80-462 steel in which a clear separation into two distinct precipitation events is not apparent. Interestingly, this steel also exhibits the highest ratio of CT to FRT (*i.e.*, high CT and relatively low FRT). As discussed previously, a high CT value will result in a larger R_2 value, while a lower FRT results in a finer R_1 value. As the log-normal mean values (R_2 and R_1) associated with each precipitation event approach each other the distributions will overlap to a greater and greater extent, such that it becomes difficult to distinguish between the two distinct distributions. X-80- 462 is unique in that it lies at the upper end of our data for CT and at the lower end of the data for FRT. Hence, the apparent unimodal precipitation observed with these samples may be due to the unique combination of processing conditions, such that the smaller precipitates associated with the lower FRT and the larger precipitate sizes associated with the higher CT mask the bimodal nature of the precipitation events.

2. *Effect of Composition*

The values of VF_2 were correlated to composition in Figures 18 and 19. Figure 18 plots VF_2 as a function of the nominal Nb to C ratio. The nominal ratio is used as the exact amounts of Nb and C available for precipitation (*i.e.*, nonequilibrium amounts are likely in solution)[7] are not known. Examination of Figure 18 does not show a definite correlation between the Nb to C composition ratio and the volume fraction of the second distribution precipitates.

Figure 19 plots VF_2 *vs* wt pct Cu, based on the possibility that some form of Cu precipitation occurs at the CT. The solubility of Cu in a Fe-Cu binary system[21] is between 0.1 and 0.2 wt pct Cu, hence, the possibility exists for some form of Cu precipitation. However, on examination of Figure 19, the relationship between volume fraction of the second precipitate distribution and wt pct Cu is inconclusive, indicating that Cu content alone does not necessarily enhance fine particle precipitation.

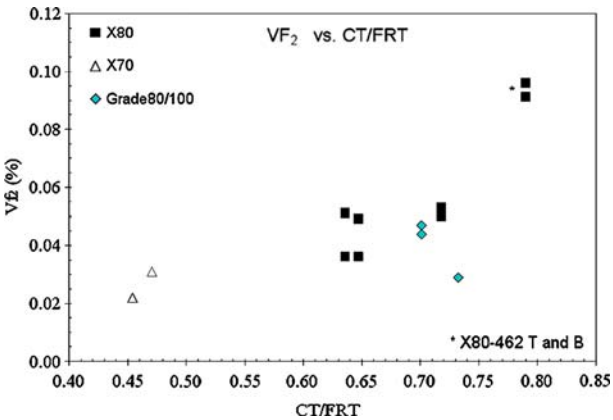

Fig. 17—Log-normal radius (VF_2) for X-70, X-80, and grades 80 and 100 as a function of the ratio of CT to FRT.

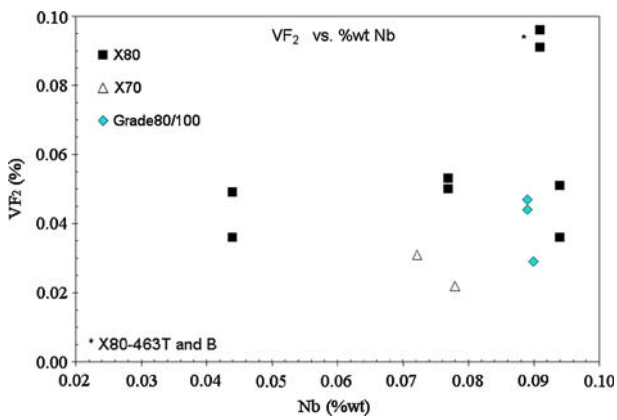

Fig. 18—Log-normal radius (VF_2) for X-70, X-80, and grades 80 and 100 as a function of the nominal Nb to C ratio.

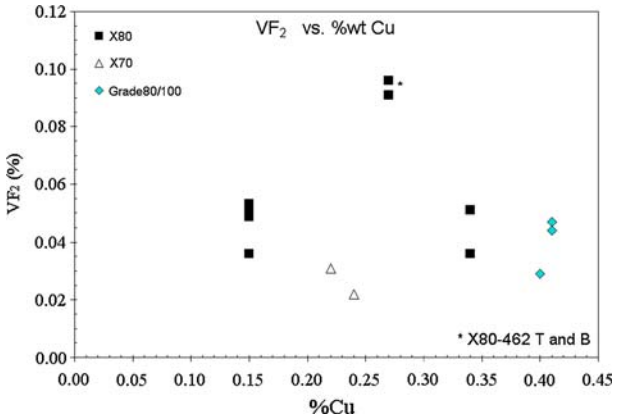

Fig. 19—Log-normal radius (VF_2) for X-70, X-80, and grades 80 and 100 as a function of the percentage of Cu.

IV. CONCLUSIONS

1. The SANS has been successfully used in quantifying precipitation characteristics of fine (nano scale) precipitates in microalloyed pipelines steels.
2. The precipitation of the fine particles (depending on processing history) was observed to occur in two distinct events—an initial (or first) event consisting of larger (and fewer) precipitates with a size range of 4 to 7 nm in diameter and a second precipitation event consisting of finer particles in the size range of 1.8 to 2.5 nm in diameter.
3. The first precipitation event exhibited decreasing size with decreasing finish rolling temperature. However, no definite correlation is observed between the first precipitation event and cooling interrupt temperature. This indicates that the fine primary precipitation occurs during finish rolling.
4. The size and volume fraction of precipitates in the second precipitation event both decrease with decreasing CT and with a decrease in the CT to FRT ratio. This indicates that the precipitation event is primarily associated with the cooling interrupt operation, but is also influenced by the FRT.
5. A decrease in CT results in a finer particle size distribution. However, in terms of strengthening, the full strengthening benefits of decreasing CT to enhance strength may not be achieved as a reduction in CT also results in a reduction in the volume fraction of these fine precipitates.
6. For the processing conditions and composition ranges of the microalloyed steel analyzed, the effect of the Nb to C ratio and the Cu content of each of the steels were individually found to have negligible effect on the volume fraction of fine precipitates that formed.

ACKNOWLEDGMENTS

The authors thank both IPSCO and NSERC for financial support. Also, the authors thank L. Collins, IPSCO, for feedback and support and J. Barker, NIST (Gaithersburg, MD), for his help with the SANS testing. The SANS facilities at the National Institute of Standards and Technology are supported by the National Science Foundation under Agreement No. DMR-9986442.

REFERENCES

1. T. Gladman: *The Physical Metallurgy of Microalloyed Steels*, Institute of Metals, London, 1997, pp. 53–55.
2. A.J. Deardo: *Int. Mater. Rev.*, 2003, vol. 48 (6), pp. 371–402.
3. S. Akhlaghi and D.G. Ivey: *Can. Metall. Q.*, 2002, vol. 41 (1), pp. 111–19.
4. S. Shanmugam, N.K. Ramisetti, R.D.K. Misra1, T. Mannering, D. Panda, and S. Jansto: *Materials Science and Technology: Recent Developments in Steel Processing*, TMS, Cincinnati, OH, 2006, pp. 829–39.
5. M. Charleux, W.J. Poole, M. Militzer, and A. Deschamps: *Metall. Mater. Trans. A*, 2001, vol. 32A, pp. 1635–47.
6. U. Sharma: Master's Thesis, University of Alberta, Edmonton, AB, Canada, 2001.
7. C. Klinkenberg, K. Hulka, and W. Beck: *Steel Res. Int.*, 2004, vol. 75 (11), pp. 744–52.
8. M.S. Gagliano and M.E. Fine: *Metall. Mater. Trans. A*, 2004, vol. 35A, pp. 2323–29.
9. S.Q. Yuan, S.W. Yang, C.J. Shang, and X.L. He: *Mater. Sci. Forum*, 2003, vols. 426–432, pp. 1307–12.
10. A. Deschamps, M. Militzer, and W.J. Poole: *ISIJ Int.*, 2001, vol. 41 (2), pp. 196–205.
11. A. Deschamps, M. Militzer, and W.J. Poole: *ISIJ Int.*, 2003, vol. 43 (11), pp. 1826–32.
12. K. Osamura, H. Okuda, S. Ochiai, M. Takashima, K. Asanao, M. Furusaka, K. Kishida, and F. Kurosawa: *ISIJ Int.*, 1994, vol. 34 (4), pp. 359–65.
13. F. Perrard, A. Deschamps, F. Bley, P. Donnadieu, and P. Maugis: *J. Appl. Crystallogr.*, 2006, vol. 39, pp. 473–82.
14. N.H. Van Dijk , S.E. Offerman, W.G. Bouwman, M. Rekvedlt, J. Sietsma, S. Van Der Zwagg , A. Bodin, and R.K. Heenan: *Metall. Mater. Trans. A*, 2002, vol. 33A (7), pp. 1883–91.
15. A.J. Allen, D. Gavillet, and J.R. Weertman: *Acta Metall.*, 1993, vol. 41 (6), pp. 1869–84.
16. P. Staron, B. Jamnig, H. Leitner, R. Ebner, and H. Clemens: *J. Appl. Crystallogr.*, 2003, vol. 36, pp. 415–19.
17. C.J. Glinka, J.G. Barker, B. Hammouda, S. Krueger, J.J. Moyer, and W.J. Orts: *J. Appl. Crystallogr.*, 1998, vol. 31, pp. 430–45.
18. A. Guinier and G. Fournet: *Small Angle Scattering of X-rays*, John Wiley and Sons, New York, NY, 1955, pp. 127–28.
19. K. Poorhaydari-Anaraki: Ph.D. Thesis, University of Alberta, Edmonton, AB, Canada, 2005.
20. B. Dutta, E.J. Palmiere, and C.M. Sellars: *Acta Mater.*, 2001, vol. 49, pp. 785–94.
21. M. Perez, F. Perrard, V. Massardier, X. Kleber, A. Deschamps, H. DeMonestrol, P. Pareige, and G. Covarel: *Philos. Mag.*, 2005, vol. 585 (20), pp. 2197–10.
22. H.J. Kestenbach, S.S. Campos, and E.V. Morales: *Mater. Sci. Technol.*, 2006, vol. 26 (6), pp. 615–26.
23. P. Riello, S. Polizzi, G. Fagherazzi, T. Finotto, and S. Ceresara: *Phys. Chem. Chem. Phys.*, 2001, vol. 3, pp. 3213–16.